THE UNIVERSITY OF
WARWICK

Original citation:
Shang, Jiangkun, Tian, Yanling, Li, Zheng, Wang, Fujun and Cai, Kunhai. (2015) A novel voice coil motor-driven compliant micropositioning stage based on flexure mechanism. Review of Scientific Instruments, 86 (9). 095001.

Permanent WRAP url:
http://wrap.warwick.ac.uk/76432

warwick**publications**wrap

highlight your research

http://wrap.warwick.ac.uk

A Novel Voice Coil Motor-driven Compliant Micropositioning Stage Based on Flexure Mechanism

Jiangkun Shang[1], Yanling Tian[1,a], Zheng Li[1], Fujun Wang[1], Kunhai Cai[1]

[1]*Key Laboratory of Mechanism Theory and Equipment Design of Ministry of Education, Tianjin University, Tianjin 300072, China*

[a] *Author to whom correspondence should be addressed.   Electronic mail: meytian@tju.edu.cn*

This paper presents a 2-DOF flexure-based micropositioning stage with a flexible decoupling mechanism. The stage is composed of an upper planar stage and four vertical support links to improve the out-of-plane stiffness. The moving platform is driven by two voice coil motors (VCMs), and thus it has the capability of large working stroke. The upper stage are connected with the base through six double parallel four-bar linkages mechanisms, which are orthogonally arranged to implement the motion decoupling in the x and y directions. The vertical support links with serially connected hook joints are utilized to guarantee good planar motion with heavy-loads. The static stiffness and the dynamic resonant frequencies are obtained based on the theoretical analyses. Finite element analysis (FEA) is used to investigate the characteristics of the developed stage. Experiments are carried out to validate the established models and the performance of the developed stage. It is noted that the developed stage has the capability of translational motion stroke of 1.8 mm and 1.78 mm in working axes. The maximum coupling errors in the x and y directions are 0.65% and 0.82%, respectively and the motion resolution is less than 200 nm. The experimental results show that the developed stage has good capability for trajectory tracking.

I. INTRODUCTION

Micro/nanopositioning techniques play significant roles in the field of medical and engineering applications, such as micromanufacturing [1], biomedical science [2], scanning electron microscopy [3] and lithography [4]. Unfortunately, most of traditional micro/nanopositioning stages have small motion strokes (usually less than 1mm) and couldn't meet the requirements of the rapid development of micro/nano related academic research and engineering applications.

Many piezo-driven stages have been designed because the piezoelectric actuators have many advantages including high-resolution, wide bandwidth and compact size [5-8]. However, the piezo-driven mechanisms have some shortcomings including short strokes, inherent hysteresis and creep nonlinearities, making it difficult and to obtain high precision positioning with large motion stroke [9-10]. Thus, in order to achieve a large motion

range, electromagnetic actuators are often selected as the actuation units [11-12]. These types of actuators are lubrication free and vacuum compatible. As a kind of electromagnetic actuators, voice coil motor(VCM) has been used in the long stroke positioning stages extensively. For example, in order to get the long stroke and high resolution, a VCM and a piezoelectric stack actuator were employed to drive the micropositioning stage as the coarse and fine drives [13-14], respectively. However, the interference behavior exists between the VCM and piezoelectric actuators. Therefore, there are several long stroke positioning stages driven by VCMs reported in [15-16]. Compared with piezoelectric actuators, VCMs can deliver a long stroke with a fine resolution easier.

Although the long stroke with a fine resolution can be generated by suitable VCMs, it is a challenge to design a suitable structure with a long stroke and fine resolution. In the structural design of micro/nanopositioning stage, wheel/rail sliding contact, wheel/rail rolling contact and aerostatic slideway are often used in previous works. However, using slide way leads to a big volume and low resolution. In addition, the maintenance cost of slide way is relatively high [17-19]. As a consequence, flexure-based mechanisms have been extensively used as the motion guide for the stage to guarantee the output precision [20-23]. The flexure-based mechanisms deliver motion by use of material elastic deformations [24-26]. As a result, they offer several advantages such as smooth displacement without backlash, friction, noise and easy manufacture [27]. However, cross-axis coupling existing in flexure-based mechanisms causes complexity modeling and controlling [28]. Development of the decoupled parallel mechanisms, which have negligible cross-axis coupling motion, is one of the solutions to eliminate such shortcoming from the mechanical design aspect. In addition, the parallel mechanisms have the advantages such as low inertia, high accuracy and identical behaviors in each axis [29-30].

In addition, for an XY stage under a large payload, structural integrity should be maintained. The out-of-plane payload that can be supported by the output platform of the stage in Ref. [14] was carried out by FEA which indicated the stiffness of the out-of-plane was about 5×10^5 N/m. Compared with the stiffness of 2.05×10^4 N/m in the working direction, the stiffness of the out-of-plane had an influence on the resolution. It is general to use aerostatic strategy or increase the thickness of the flexure, which will increase cost or difficulty in machining, to enhance the out-of-plane stiffness [31-32]. Therefore, spatial compliant mechanisms are applied to improve the out-of-plane stiffness. An XY compliant parallel mechanism (CPM) has been designed by Hao et al [32]. It has a large range and spatial compliant mechanisms to enhance the out-of-plane stiffness. But the feasibility of the design was only confirmed from the theoretical analysis.

This paper proposes a novel flexure-based precision positioning stage, which has a millimeter motion range, enhanced out-of-plane stiffness, parallel kinematics, and totally decoupled motion. This paper focuses on the

mechanical design, theoretical modeling and analyses, and experimental verification. The reminder of the paper is organized as follows: Section II presents the mechanical design of the XY stage. In section III, compliance modeling method is utilized to analyze the stage and the parameters of the positioning stage are determined based on theoretical analysis. FEA is utilized to verify the static and dynamic characteristics of the developed stage. In section IV, the performance of the developed stage has been examined. Finally, conclusions are given in section V.

II. DESIGN OF XY STAGE

A novel large working range and payload capability XY CPM is evolved from the 4PP-E (P stands for prismatic joint and E denotes planar joint) decoupled parallel mechanism based on the following principles: (a) to obtain a large motion range, (b) a simple configuration and (c) approximately negligible out-of-plan motion in the z axis and (d) ensure decoupling translation motions along working axes.

As shown in Fig.1, the designed XYCPM mainly consists of an upper stage, four vertical support links, a base and two VCMs. In the upper stage, the double parallel four-bar linkages mechanisms are symmetrically arranged to realize decoupling and large motion range. The hook compliant series mechanism (HCSM) used as vertical support links is designed to guarantee excellent out-of-plane stiffness for heavy payload. The basic unit of HCSM is hook joint shown in Fig.2 (a). Each hook joint is composed of two circular hinges and the axes of these circular hinges are located in one plane for a compact physical dimension. HCSM consists of four legs and each leg is made of two hook joints in series as shown in Fig.2 (b). In this case, the out-of-plane motions, including rotation about the x and y axes or translation in the z axis, are suppressed. Furthermore, the center of the moving platform coincides with the stiffness center of the HCSM, and thus minimizes the parasitic motion. Therefore, the stage can realizes a large motion range, enhanced out-of-plane stiffness and small coupling error.

III. MODELING

A. Output compliance modeling

Since the flexure-based mechanisms work in the elastic deformation region, it is assumed that relationship between loads and displacements are linear. When force and moments are applied on a certain point as shown in Fig.3 (a), the following equation is established:

$$X = CF \tag{1}$$

where $X=[\delta_x, \delta_y, \delta_z, \theta_x, \theta_y, \theta_z]$, $F=[f_x, f_y, f_z, M_x, M_y, M_z]$, and C can be derived from Ref. [33]

$$C = \begin{bmatrix} c_1 & 0 & 0 & 0 & c_3 & 0 \\ 0 & c_2 & 0 & -c_4 & 0 & 0 \\ 0 & 0 & c_5 & 0 & 0 & 0 \\ 0 & -c_4 & 0 & c_6 & 0 & 0 \\ c_3 & 0 & 0 & 0 & c_7 & 0 \\ 0 & 0 & 0 & 0 & 0 & c_8 \end{bmatrix} \tag{2}$$

where c_i (i=1, 2,…8) are shown in Table 1 in case of prismatic beam and right circular notched hinge. The E^* denotes Young's modulus for planar strain and G is the shear modulus. The other parameters are shown in Fig.2.

The compliance matrix of a flexure can be transformed from its local coordinate o_i-xy to another coordinate o_j-xy by

$$C_j = R_i P(r_i) C_i P(r_i)^\text{T} R_i^\text{T} \tag{3}$$

where R_i is defined as the orientation matrix of o_i-xy with respect to o_j-xy and R_i is also known as the direction cosine matrix; $P(r_i)$ denotes the translation matrix, and can be described as follows:

$$P(r_i) = \begin{bmatrix} I_{3\times3} & \begin{matrix} 0 & -z_i & y_i \\ z_i & 0 & -x_i \\ -y_i & x_i & 0 \end{matrix} \\ O_{3\times3} & I_{3\times3} \end{bmatrix} \tag{4}$$

where $I_{3\times3}$ and $O_{3\times3}$ are separately 3×3 identity matrix and zero matrix; $r_i = [x_i, y_i, z_i]^\text{T}$ is the position vector of the point o_j that is expressed in the reference frame of o_i-xy. To obtain the compliance matrix of the whole stage, the local compliance matrices of all flexures should be transformed to the center point of the moving platform.
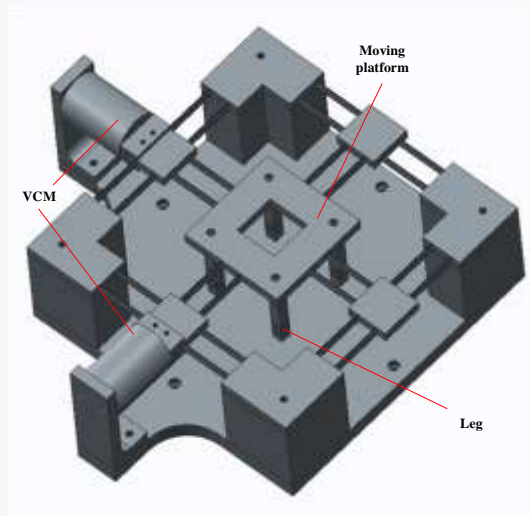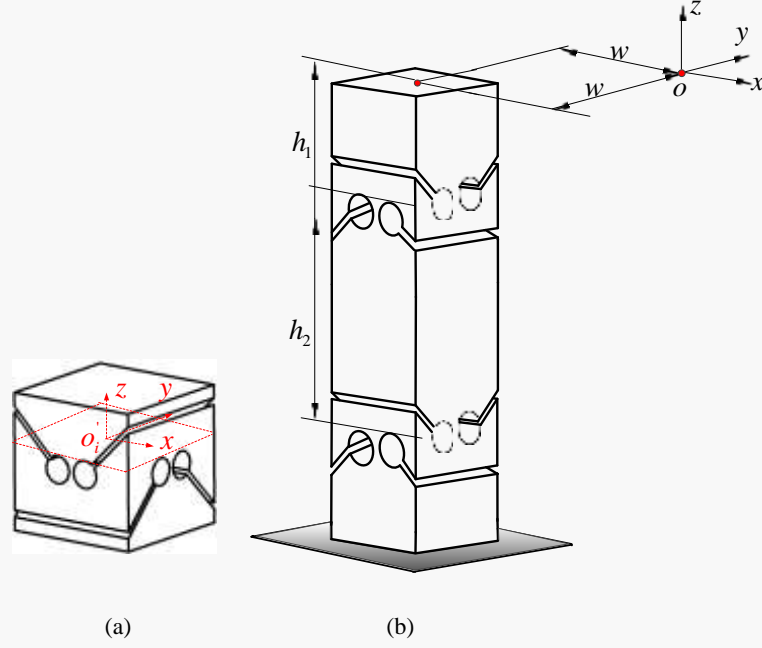

FIG.1. A novel XY CPM.

(a)   (b)

FIG.2 (a) Hook joint (b) leg

TABLE I. Compliance matrices of beam and hinge.

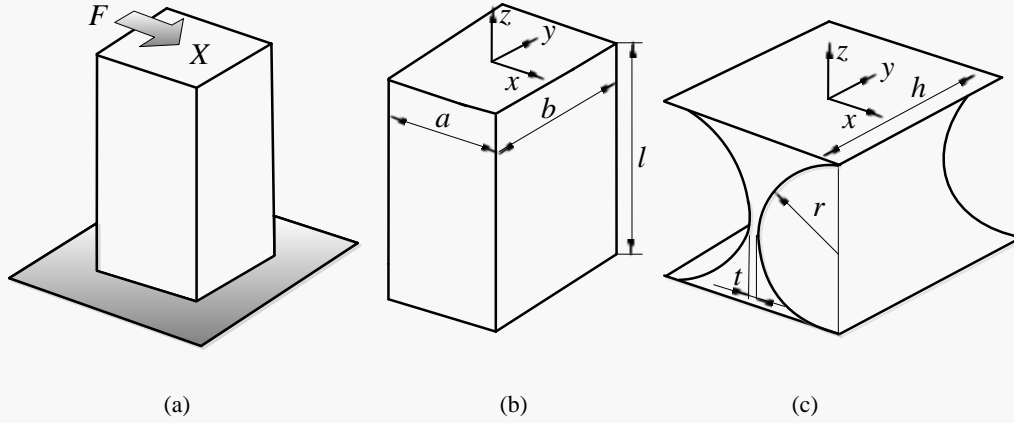| Parameters	Prismatic beam	Right circular notched hinge	Parameters	prismatic beam	Right circular notched hinge
c_1	$\dfrac{4l^3}{E^*a^3b}$	$\dfrac{9\pi r^{\frac{5}{2}}}{2E^*ht^{\frac{5}{2}}}+\dfrac{3\pi r^{\frac{3}{2}}}{2E^*ht^{\frac{3}{2}}}$	c_5	$\dfrac{l}{E^*ab}$	$\dfrac{1}{E^*h}\left\{\pi(\dfrac{r}{t})^{\frac{1}{2}}-\dfrac{\pi}{2}\right\}$
c_2	$\dfrac{4l^3}{E^*ab^3}$	$\dfrac{12\pi r^2}{E^*h^3}\left\{(\dfrac{r}{t})^{\frac{1}{2}}-\dfrac{1}{4}\right\}$	c_6	$\dfrac{12l}{E^*ab^3}$	$\dfrac{12}{E^*h^3}\left\{\pi(\dfrac{r}{t})^{\frac{1}{2}}-\dfrac{2+\pi}{2}\right\}$
c_3	$\dfrac{6l^2}{E^*a^3b}$	$\dfrac{9\pi r^{\frac{3}{2}}}{2E^*ht^{\frac{5}{2}}}$	c_7	$\dfrac{12l}{E^*a^3b}$	$\dfrac{9\pi r^{\frac{1}{2}}}{2E^*ht^{\frac{5}{2}}}$
c_4	$\dfrac{6l^2}{E^*ab^3}$	$\dfrac{12r}{E^*h^3}\left\{\pi(\dfrac{r}{t})^{\frac{1}{2}}-\dfrac{2+\pi}{2}\right\}$	c_8	$\dfrac{l}{Gk_2a^3b}$	$\dfrac{9\pi r^{\frac{1}{2}}}{2Ght^{\frac{5}{2}}}$

FIG.3. (a) Load sketch (b) prismatic beam hinge and (c) parameters of right circular notched hinge.
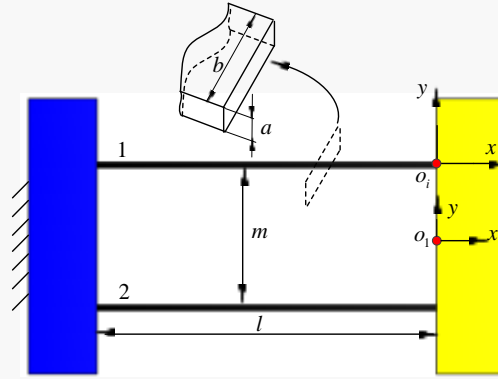

FIG.4. Dual-beam parallelogram module.

The planar dual-beam parallelogram module in the compliance P joint of the XY CPM is shown in Fig.4. We can obtain the compliance matrix of flexure hinge1 in coordinate frame o_1-xy as follows:

$$C_1 = P(r_1)CP(r_1)^{\mathrm{T}} \tag{5}$$

where $r_1 = [0, -m/2, 0]^{\mathrm{T}}$. Flexure hinges 1 and 2 are symmetric with respect to x axis. Hence the compliance matrix of flexure hinge 2 in coordinate frame o_1-xy can be obtained by rotating the compliance matrix of flexure hinge 1 by π about x axis

$$C_2 = R_x(\pi)C_1R_x(\pi)^{\mathrm{T}} \tag{6}$$

Flexure hinges 1 and 2 are connected in parallel, the compliance of the two-beam parallelogram module can be written by

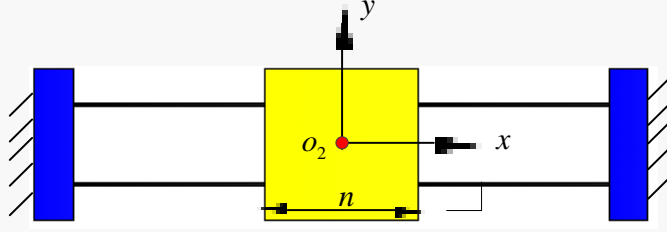$$C_s = ((C_1)^{-1} + (C_2)^{-1})^{-1} \tag{7}$$

FIG.5. Double parallel four-bar linkages mechanism.

Thus, the compliance matrix of the double parallel four-bar linkages mechanism shown in Fig.5, which is composed of two planar dual-beam parallelogram modules, can be expressed in coordinate frame o_2-xy as

$$C_d = \left[(C_{s1})^{-1} + (C_{s2})^{-1} \right]^{-1} \tag{8}$$

where C_{s1} is the compliance matrix of left side dual-beam parallelogram module in the coordinate frame o_2-xy; C_{s2} is the right one, which can be calculated by rotating compliance matrix C_{s1} by π about y axis

$$C_{s1} = P(r_2)C_s P(r_2)^{\mathrm{T}} \tag{9}$$

$$C_{s2} = R_y(\pi)C_{s1}R_y(\pi)^{\mathrm{T}} \tag{10}$$

where $r_2 = [n/2, 0, 0]^{\mathrm{T}}$.

Then the compliance matrix of compound dual-beam parallelogram module, which is composed of a dual-beam parallelogram module and a double parallel four-bar linkages mechanism in series shown in Fig.6, can derived in the coordinate frame o_3-xy by

$$C_c = R_z(-\frac{\pi}{2})C_d R_z(-\frac{\pi}{2})^{\mathrm{T}} + P(r_3)C_s P(r_3)^{\mathrm{T}} \tag{11}$$

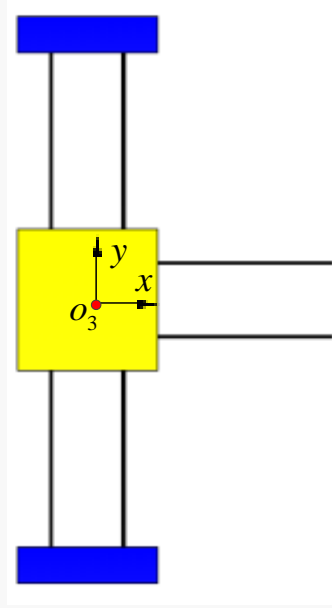where $r_3 = [-(n/2+l), 0, 0]^{\mathrm{T}}$.

FIG.6. Compound two-beam parallelogram module.

Since a 4PP XY CPM is made of four compound dual-beam parallelogram modules connected in parallel as shown in Fig.7, the compliance matrix can be obtained as follows:

$$C_u = [(C_{c1})^{-1} + (C_{c2})^{-1} + (C_{c3})^{-1} + (C_{c4})^{-1}]^{-1} \qquad (12)$$

where C_{c1} is the compliance matrix of section 1 which can be derived from

$$C_{c1} = P(r_4)C_c P(r_4)^{\mathrm{T}} \qquad (13)$$

where $r_4 = [u,0,0]^{\mathrm{T}}$; by rotating C_{c1} $\pi/2$, π and $3\pi/2$ around z axis, the compliance matrix of other sections can be derived as follows:

$$\begin{cases} C_{c2} = R_z(\frac{\pi}{2})C_{c1}R_z(\frac{\pi}{2})^{\mathrm{T}} \\ C_{c3} = R_z(\pi)C_{c1}R_z(\pi)^{\mathrm{T}} \\ C_{c4} = R_z(\frac{3\pi}{2})C_{c1}R_z(\frac{3\pi}{2})^{\mathrm{T}} \end{cases} \qquad (14)$$

For a hook joint is composed of two circular hinges in series, the compliance matrix of a hook joint in its own local coordinate shown in Fig.2 (a) can be defined by

$$C_h = \{C^{-1} + [R_z(\frac{\pi}{2})CR_z(\frac{\pi}{2})^{\mathrm{T}}]^{-1}\}^{-1} \qquad (15)$$

where C is the local compliance matrix of the right circular hinge [Eq. (2)], and the parameter h should be replaced by $(h-4r)$ for the sake of transfixion. The compliance matrix of leg shown in Fig.2 (b) can be known by

$$C_{leg1} = [P(r_5)C_h P(r_5)^{\mathrm{T}}]^{-1} + [P(r_6)C_h P(r_6)^{\mathrm{T}}]^{-1} \qquad (16)$$
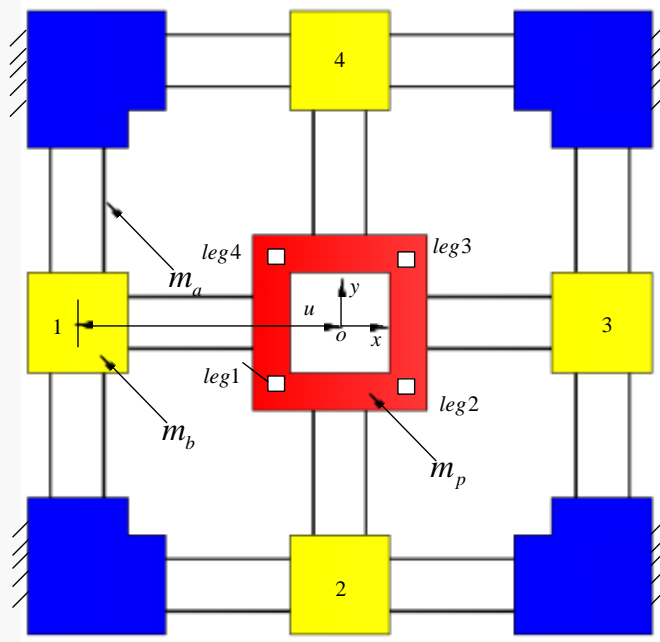
where $r_5 = [w, w, h_1]$, $r_6 = [w, w, h_1 + h_2]$.

FIG.7. 2-DOF positioning stage.

According to the relationships among these legs, the compliance matrices can be derived as

$$\begin{cases} \boldsymbol{C}_{leg2} = \boldsymbol{R}_y(\pi)\boldsymbol{C}_{leg1}\boldsymbol{R}_y(\pi)^\mathrm{T} \\ \boldsymbol{C}_{leg3} = \boldsymbol{R}_x(\pi)\boldsymbol{C}_{leg2}\boldsymbol{R}_x(\pi)^\mathrm{T} \\ \boldsymbol{C}_{leg4} = \boldsymbol{R}_y(\pi)\boldsymbol{C}_{leg1}\boldsymbol{R}_y(\pi)^\mathrm{T} \end{cases} \tag{17}$$

Therefore, the compliance matrix of HCSM can be given as

$$\boldsymbol{C}_l = [(\boldsymbol{C}_{leg1})^{-1} + (\boldsymbol{C}_{leg2})^{-1} + (\boldsymbol{C}_{leg3})^{-1} + (\boldsymbol{C}_{leg4})^{-1}]^{-1} \tag{18}$$

The whole positioning stage is composed of 4PP XY CPM and HCSM in parallel, so the compliance matrix of the XYCPM can be obtained as

$$\boldsymbol{C}_{out} = [(\boldsymbol{C}_u)^{-1} + (\boldsymbol{C}_l)^{-1}]^{-1} \tag{19}$$

B. Dynamic modeling

A high resonant frequency is desired to generate a high bandwidth of the system, so it is necessary to analysis the resonant frequency of the stage.

Based on Lagrange's equation, the free-motion of the XY stage can be written as follows:

$$\frac{d}{dt}(\frac{\partial T}{\partial \dot{x}}) - \frac{\partial T}{\partial x} + \frac{\partial V}{\partial x} = F \tag{20}$$

where T, V, t and x represent the kinetic energy, the potential energy, time and displacement in working direction, respectively. Then the kinetic energy of the stage is calculated as

$$T = \frac{1}{2} M \dot{x}^2 \tag{21}$$

where M is the equivalent mass obtained by

$$M = m_p + 2m_b + 4m_a + 12m_a(\frac{1}{2})^2 + 12I_g(\frac{1}{l})^2 +$$

$$4\left\{ m_3\left(\frac{0+\frac{1}{2}}{2}\right)^2 + m_2\left(\frac{1}{2}\right)^2 + m_3\left(\frac{\frac{1}{2}+1}{2}\right)^2 + m_1 + 4I_g{}'\left(\frac{1}{h_2}\right)^2 \right\} \tag{22}$$

where m_a denotes the mass of cantilever beam; m_b is the mass of the linker (the yellow part) shown in Fig.5; m_p denotes the mass of output stage; and the significances of m_1, m_2, m_3 is shown in Fig.8. It is noted that the volume of m_1, m_2, m_3 are calculated by software.
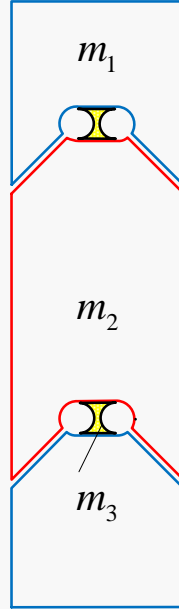
FIG.8. Schematic diagram of column mass distribution.

The potential energy can be computed by

$$V = \frac{1}{2} K_r x^2 + \frac{1}{2} K_r{}' x^2 \tag{23}$$

where K_r and $K_r{}'$ is the equivalent stiffness of the upper stage and the equivalent stiffness of HCSM, respectively, which can be derived from C_u and C_l.

The free-motion dynamics equation can be determined by substituting Eqs. (21), (22) and (23) into Eq. (20)

$$M\ddot{x} + (K_r + K_r{}')x = 0 \tag{24}$$

Then, based on the theory of vibrations, the resonant mode frequency can be computed as

$$f_x = \frac{1}{2\pi} \sqrt{\frac{K_r + K_r{}'}{M}} \tag{25}$$

C. Parameters design

Based on maximal shear stress theory, the actual transverse end-deflections for the beams both in the P joint and hook joint should meet the following conditions [34]:

$$\begin{cases} \Delta_1 = \dfrac{1}{3\eta} \dfrac{\sigma}{E} \dfrac{l^2}{b} \\ \Delta_2 = \dfrac{1}{3\eta} \dfrac{\sigma}{E} \dfrac{h_2^2}{t} \end{cases} \tag{26}$$

where Δ_1, Δ_2 are the actual transverse end-deflections for P joint and hook joint, respectively; η is the safety factor. To achieve a motion of 1.8mm along each working axis, the equation can be obtained

$$\begin{cases} \dfrac{l^2}{b} \geqslant \dfrac{3 \times 1.8 \times 10^{-3} \eta E}{\sigma} \\ \dfrac{h_2^2}{t} \geqslant \dfrac{3 \times 1.8 \times 10^{-3} \eta E}{\sigma} \end{cases} \tag{27}$$

In addition, the slender leaf springs with a relatively high ratio of length to thickness should bear the compressive load, which may be prone to elastic buckling. This phenomenon will have a serious influence on the positioning resolution and coupling error, therefore the buckling should be avoided by the structure design. The critical axial load causing elastic buckling can be obtained by

$$P_{cr} = \frac{\pi^2 EI}{l_{cr}^2} \tag{28}$$

where l_{cr} is the effective length of flexure and expressed by

$$l_{cr} = kl \tag{29}$$

where k is the coefficient decided by boundary condition, range from 0.5 to 2. In order to avoid the elastic buckling, the stage should meet

$$F_{VCM} \leqslant P_{cr} \tag{30}$$

i.e.,

$$F_{VCM} \leqslant \frac{p^2 Ebh^3}{12l_{cr}^2} \tag{31}$$

According to Eq.(27) and (31) and the manufacturability requirement, the parameters of the structure are

designed in Table II.

<div align="center">TABLE II. The parameters of the positioning stage.</div>

Parameters	l	a	b	m	n	u
Value(mm)	50	10	0.5	20	40	120
Parameters	h	h_1	h_2	w	r	t
Value(mm)	10	14	40	35	1	0.4

D. Finite element analyses

In the finite element analysis (FEA) simulations, the alloy material of Al 7075 is defined to the stage. Table III shows the parameters of the material used to the stage. In simulation, the base of the stage and the four corners of the upper planar stage are fixed. Based on the working condition, the FEA results of the first three natural frequencies are shown in Table III, and the mode shapes are depicted in Fig.9. The first and second mode shapes are translations along two working axes, respectively. The third mode shape is a rotation about the z axis. As shown in Table IV, the first two resonant frequencies have little difference, but the third resonant frequency is ten times more than the first two frequencies. It demonstrates a robust translational motion along the working directions.

<div align="center">TABLE III. The parameters of the material.</div>

Young's modulus	Yield strength	Poisson's ratio	Density
70GPa	434MPa	0.34	$2.7 \times 10^3 \text{kg/m}^3$

<div align="center">TABLE IV. Natural frequency of the micropositioning stage.</div>

Mode	1	2	3
Theoretical(Hz)	46.99	46.99	-
FEA(Hz)	48.05	48.28	434.27
Error (%)	2.26	2.74	-

FEA simulations are carried out to assess the out-of-plane payload capacity of the developed stage. The surface load of 10N in the z direction is applied on the moving platform, and the maximum displacement is only about 0.315μm as shown in Fig.10 (a). As a comparison, the Fig.10 (b) shows, with the same load applied on the moving platform, the introduced displacement of the stage without HCSM is 32.876 μm, which is about 100 times more than the displacement with HCSM. This indicates that the out-of-plane stiffness is 3.175×10^4 N/mm and 3.04×10^2 N/mm, respectively and thus the payload capability can be improved significantly by using HCSM.

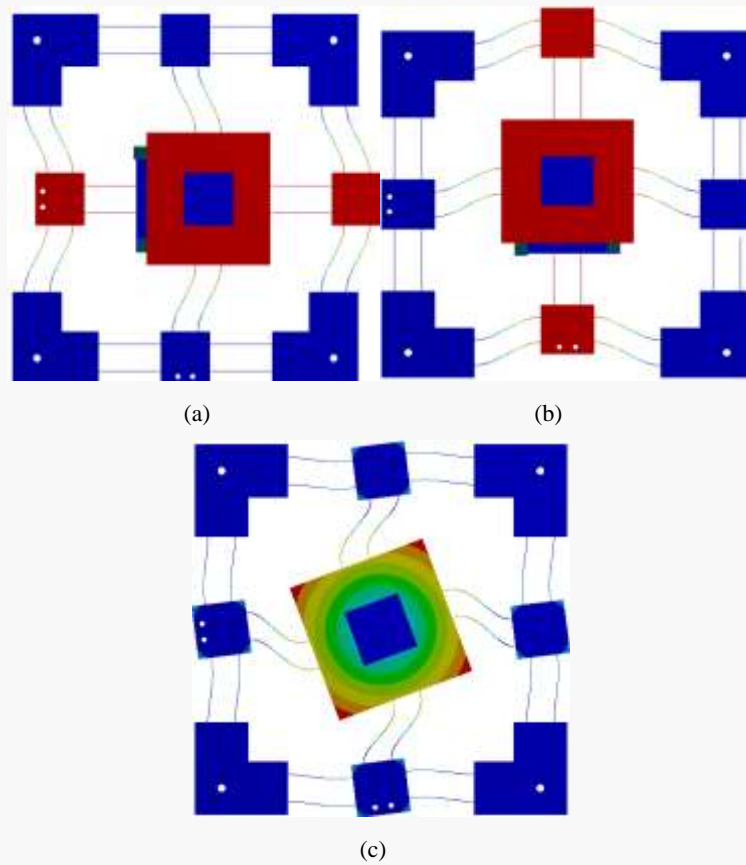(a)   (b)

(c)

FIG.9. The first three mode shapes of the micropositioning stage.(a) first mode shape (b) second mode shape and (c)
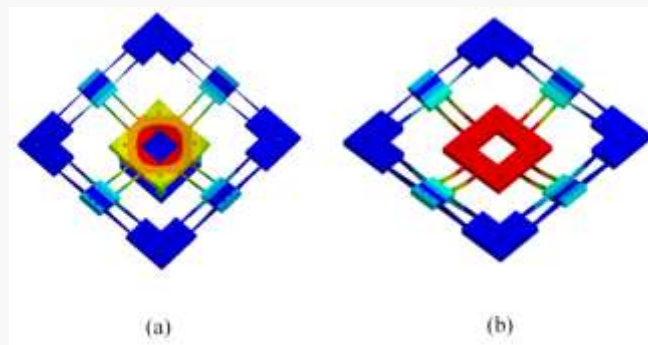
third mode shape.

FIG.10. The total deformation of the stage. (a) with HCSM and (b) without HCSM.

IV. EXPERIMENT TESTS

In order to demonstrate the feasibility of the design XY stage, the performances are verified by a series of experimental studies in this section.

A. Stiffness test

The 2-DOF precision positioning stage requires suitable bandwidth and stiffness simultaneously. It is necessary to test the stiffness of the XY stage which has been manufactured using the WEDM technique. The

setup of the stiffness experiment platform is shown in Fig.11. The experiments were all going on a Newport RS-4000optical table so as to reduce the effect of disturbances. A force gauge (NK-20) is used to test the force on the stage, and a displacement sensor (TESA-04430011) is used to get the translation range when the force gauge pushes the stage along two working and z axes, respectively.

Three group of the experiment have been done along per axis, and linear interpolation is used to fitting the experimental data. The results of the stiffness experiment are shown in Fig.12 and the value of the stiffness is shown in Table V. It is noted that the FEA results are in good agreement with the theoretical results. This indicates that the model used in theoretical analysis is correct. The comparison between the FEA results and experiment ones shows the error of z axis is 9.38%. This may be caused by the contact region between the upper stage and HCSM.
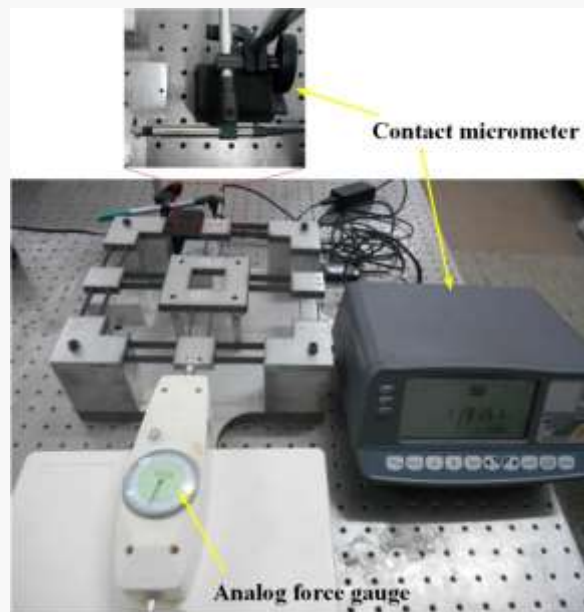

FIG.11. Stiffness experiment platform

TABLE V. The stiffness of the micropositioning stage

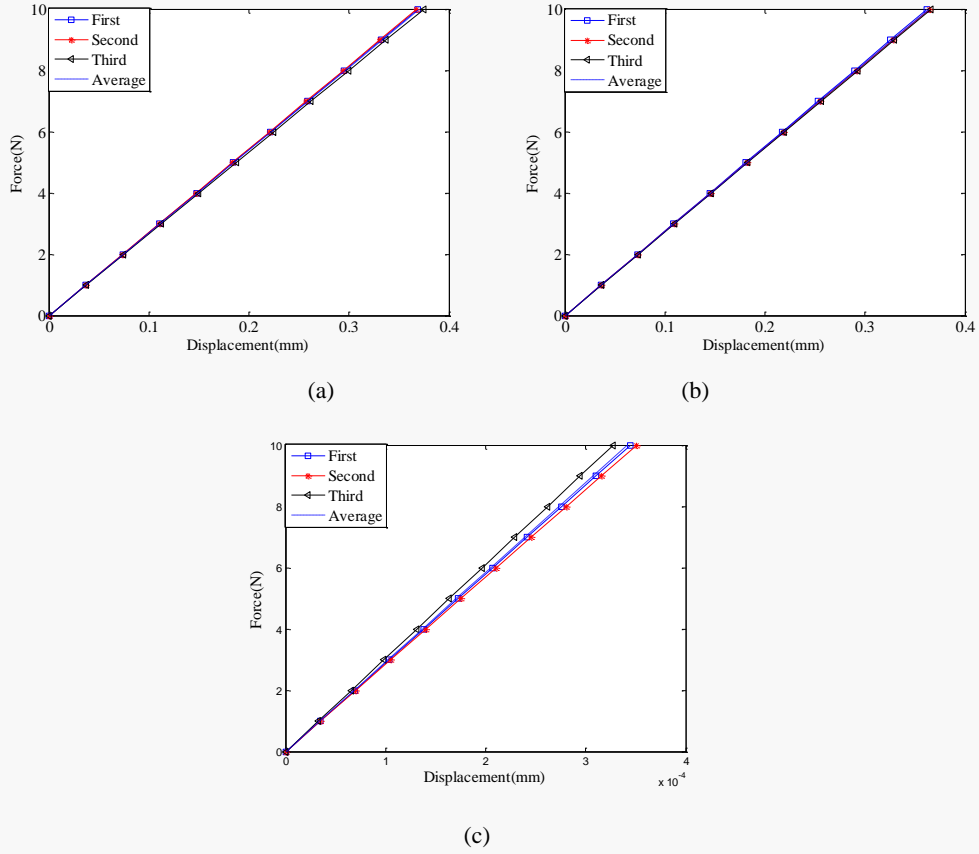| Stiffness	x	y	z
FEA(N/mm)	28.6	29.2	3.20×10^4
Theoretical(N/mm)	28.12	28.12	-
Experiment(N/mm)	27.0	27.5	2.93×10^4
Error(%)	5.92	6.18	9.38

(a)

(b)

(c)

Fig.12. Stiffness results in the (a) *x* axis (b) *y* axis and (c) *z* axis

B. Modal analyses

Modal analysis is conducted to investigate the dynamics performance of the developed stage. The experimental setup is shown as Fig.13. The dynamic analyzer system consists of an acceleration transducer, a TST-511F002 hammer, a B&K2692 charge amplifier, a TJDAS test system and a computer. To reduce the effect of the vibration and noise, the experiment is carried out on a Newport RS-4000 optical table. In the experiment the natural frequencies of working axes are measured by transient measurement method respectively. As it is shown in Fig.14, the natural frequencies are 35.62 Hz and 35.82 Hz, respectively. Compared with the calculated value of $f_x = f_y = 46.99$ Hz, the error is 31.99% and 31.18%, respectively. It is mainly caused by the acceleration transducer mass, which is 0.06 kg. Thus, the theoretical value of the stage including the mass of the acceleration transducer is calculated and the value is 39.48 Hz, which has the error of 10.83% and 10.21%.
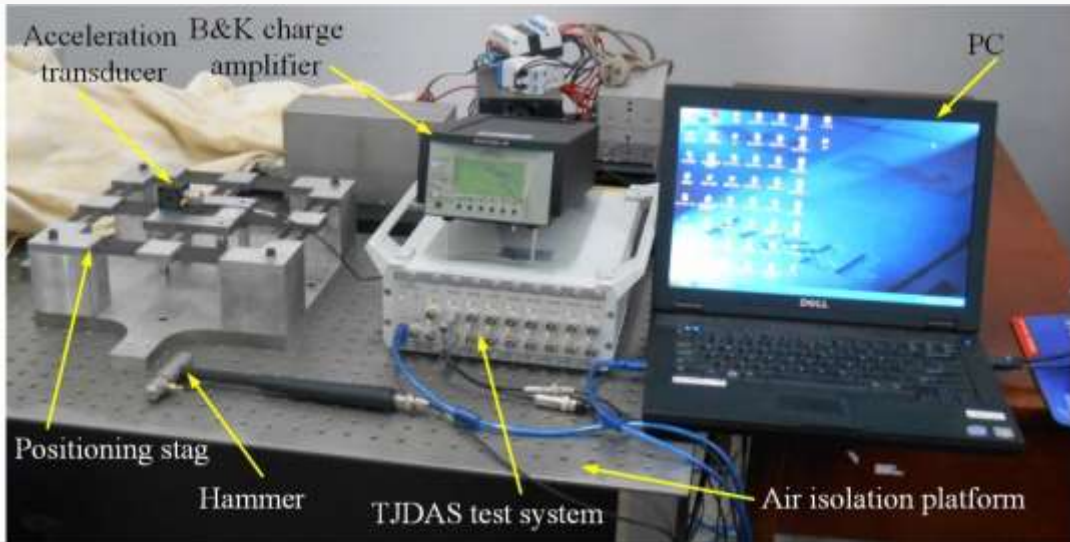
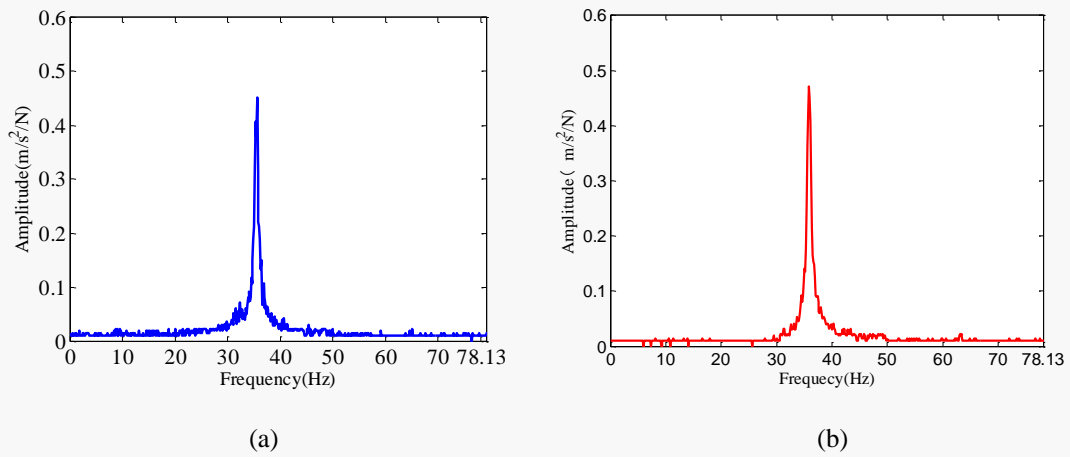FIG.13. The natural frequency test of micropositioning stage.

| (a) | (b) |

FIG.14. Frequency spectrogram of the micropositioning stage. (a) *x* axis and (b) *y* axis.

C. Modal analyses motion characteristic test

Fig.15 shows the experiment setup for the trajectory tracking test. In order to meet the demand of a large motion range, two VCMs (NCC05-18-060-2X), with a maximum driving force of 80.1N, are used to drive the stage, and two linear servo amplifiers(LCAM 5/15, from H2W Corporation) are employed to drive the VCMs. Two laser displacement sensors (KEYENCE LK-H050) with a resolution of 25 nm within the measurement range of ±10 are utilized to measure the position output. A dSPACEDS1103 R&D control board is utilized to implement signals output accurately.
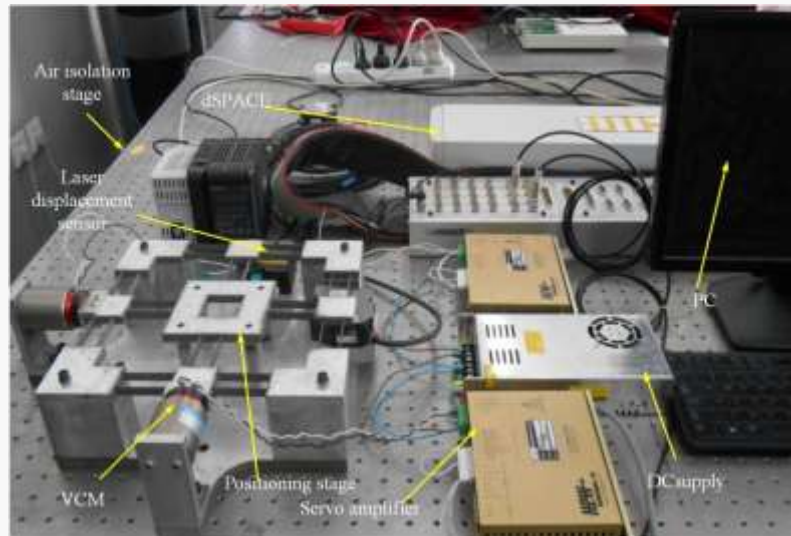
FIG.15. Trajectory tracking test setup

To study the motion performance of the micropositioning stage, the sinusoidal signal response tests are carried out. As shown in Fig.16, the maximum displacements in the x and y directions are 1.8mm and 1.78mm, respectively. Fig.17 shows the hysteresis loops and the corresponding coupling errors. The maximum coupling errors are 0.65% and 0.82% which reveals the decoupling of the stage is quite reliable. The difference between the two axes is mainly caused by machining and measurement errors.
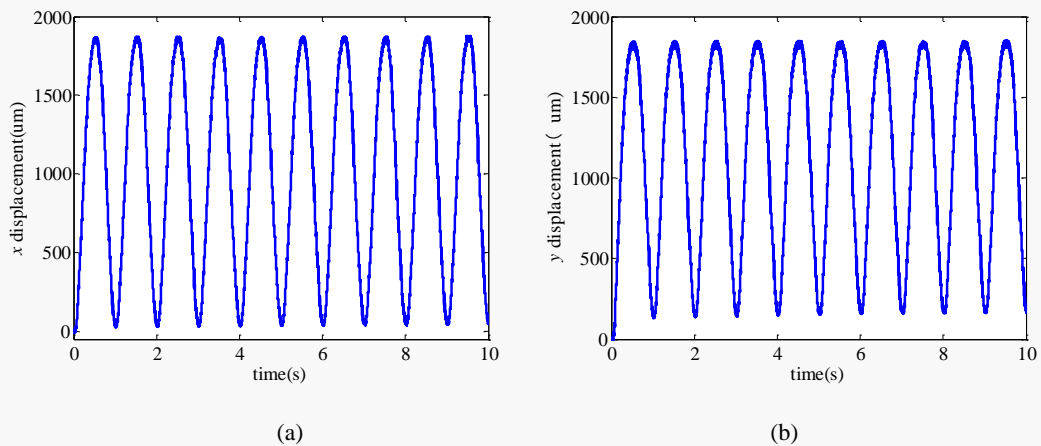

(a)

(b)

FIG.16. The sinusoidal signal responses of the micropositioning stage. (a) x axis and (b) y axis.
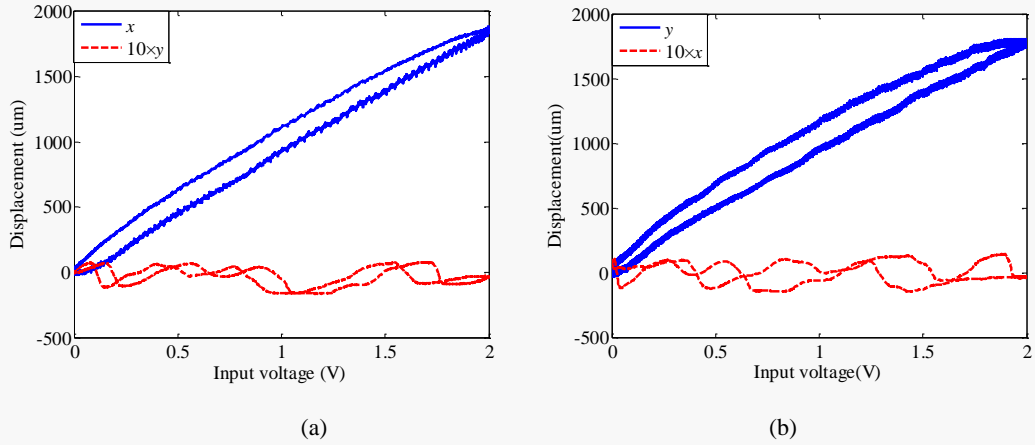
FIG.17. Hysteresis loops and coupling errors of the micropositioning stage. (a) *x* axis and (b) *y* axis.

In order to examine the dynamic response capability of the micropositioning stage, through the D/A converter board, the digital computer generates a step signal and supplies to the DC supply which supplies electric current to the VCMs. Moreover, an open loop and a closed loop PI (proportion integration) control are employed to control the system, respectively. The experiment results are shown in Fig.18 (a) and (b). It is observed that settling times in open loop control for the *x* and *y* axes are 0.112s and 0.114s with a maximum overshoot 19.35% and 24.39%, respectively. The response speed is satisfied for a long stroke stage. While, with a PI control applied, the settling times reach 0.095s and 0.109s without overshoot, respectively. It reveals that the dynamic performance of the micropositioning stage can be well improved by the PI control.
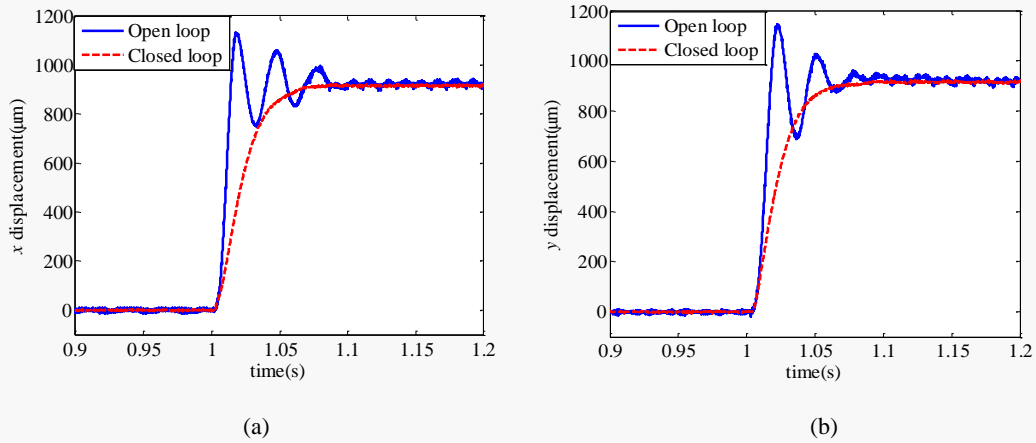

FIG.18. Step responses of the micropositioning stage. (a) *x* axis and (b) *y* axis.

To further study the properties of the stage, the resolution of the XY stage is tested by applying a consecutive step voltage. As shown in Fig.19, the minimum resolution of the micro stage is less than 200 nm. In fact, the resolution can be further improved by applying more efficiently controlling system. Moreover, the resolution and accuracy of the positioning stage depend on the employed displacement sensors.
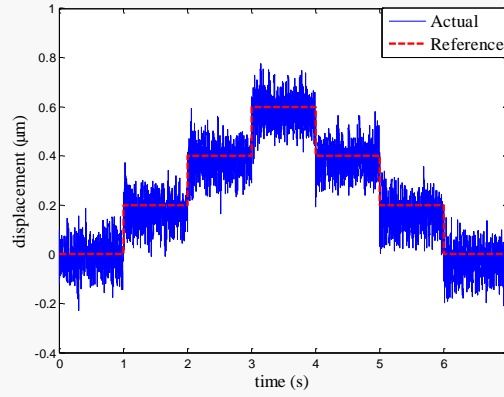
FIG.19. Resolution test of the micropositioning stage.

A circular trajectory is used to examine the tracking performance of the developed stage. The circular trajectory centered at point (400μm, 400μm) with a radius of 200 μm in the xy plane. The measured trajectory and the desired circle are plotted on Fig.20 (a). It is noted that it can follow the desired command. As it is shown in Fig.20 (b), the tracking error in the x axis is within ±6.5μm and the error in the y axis keeps within ±12.5μm. Compared with the error in the x axis, the error in the y axis is slightly larger. This may be caused by cross couplings, machining error, and measurement error of displacement sensors.

(a)   (b)
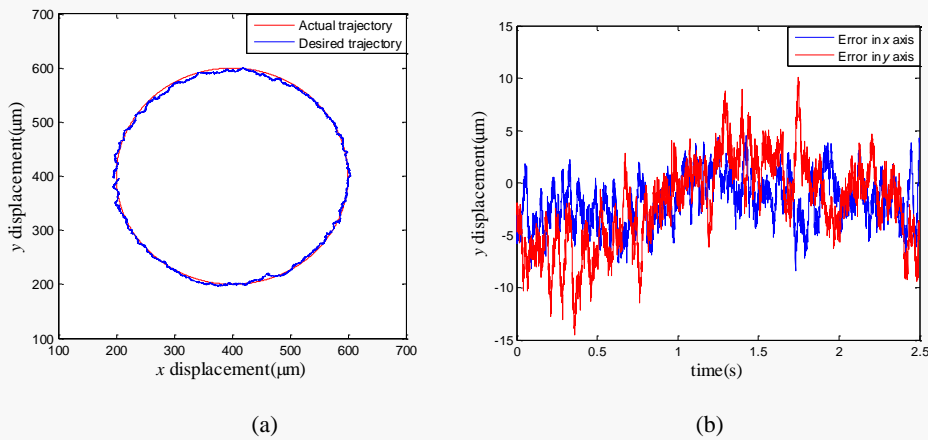
FIG.20. Tracking performance on a circular trajectory of the stage. (a) measured response (b) error in the x axis and y axis.

V. CONCLUSION

A large motion range micropositioning stage has been designed and tested. The FEA simulation results predicted the first three resonant mode frequencies and mode shapes. And the out-of-plane payload is assessed by carrying FEA simulations. A robust translational motion along the working direction is demonstrated through the comparison of the modal frequencies. And the stiffness is obtained by stiffness experiments. The

micropositioning stage has natural frequencies of 35.62 Hz and 35.82 Hz along the working axes, respectively. The sinusoidal signal response tests are carried out and a workspace of 1.8 mm×1.78 mm can be obtained. Moreover, the experimental results show the coupling errors 0.65% and 0.82% which indicates a reliable decoupled motion between two working axes. Furthermore, the resolution of 200 nm is carried out by experiment and the trajectory tracking experiment shows that the stage can achieve good performance for dynamic commands.

ACKNOWLEDGMENTS

REFERENCES

[1] Y. Tian, B. Shirinzadeh, Zhang D, G. Alici, Development and dynamic modeling of a flexure-based Scott–Russell mechanism for nano-manipulation. Mechanical Systems and Signal Processing, 2009, 23(3): 957-978.

[2] Y. Zhang, K. Tan, S. Huang, Vision-servo system for automated cell injection, IEEE Transaction on Industrial Electronics, 2009, 56(1):231-238.

[3] J. Kwon, J. Hong, Y.S. Kim, Y. Lee, D. Lee, K., Lee, S. Park, Atomic force microscope with improved scan accuracy, scan speed, and optical vision, Review of Scientific Instruments, 2003, 74(10): : 4378–4383.

[4] J. Jung, K. Huh, Simulation tool design for the two axis nano stage of lithography systems, Mechatronics, 2010, 20(5):574-581.

[5] K.-B. Choi, D. Kim, Monolithic parallel linear compliant mechanism for two axes ultra-precision linear motion. Review of scientific instruments, 2006, 77(6): 065106.

[6] Y. Li, Q. Xu, Design and Analysis of a Totally Decoupled Flexure-Based XY Parallel Micromanipulator. Robotics IEEE Transactions on, 2009, 25(3):645 - 657.

[7] Y. K. Yong, S. Aphale, S. O. R. Moheimani, Design, identification, and control of a flexure-based XY stage for fast nanoscale positioning. Nanotechnology, IEEE Transactions on, 2009, 8(1): 46-54.

[8] C.-M. Wen, M.Y. Cheng, Development of a recurrent fuzzy CMAC with adjustable input space quantization and self-tuning learning rate for control of a dual-axis piezoelectric actuated micromotion stage. Industrial Electronics, IEEE Transactions on, 2013, 60(11): 5105-5115.

[9] Q. Xu, Identification and compensation of piezoelectric hysteresis without modeling hysteresis inverse. Industrial Electronics, IEEE Transactions on, 2013, 60(9): 3927-3937.

[10] S. Awtar, G. Parmar, Design of a large range XY nanopositioning system. Journal of Mechanisms and Robotics, 2013, 5(2): 021008.

[11] J. Kindblom, A.M. Ekelund-Olvenmark, H. Syren, R. Iustin, K. Braide, I. Frank-Lissbrant, B. Lennernäs, High precision transponder localization using a novel electromagnetic positioning system in patients with localized prostate cancer. Radiotherapy and Oncology, 2009, 90(3): 307-311.

[12] M.U. Khan, N. Bencheikn, C. Prelle, T. Beutel, S. Buttgenbach, A Long Stroke Electromagnetic Positioning Stage for Micro

Applications. Mechatronics, IEEE/ASME Transactions on, 2012, 17(5): 866-875.

[13] W. Dong, J. Tang, Y. Eldeeb. Design of a linear-motion dual-stage actuation system for precision control. Smart Materials & Structures, 2009, 18(9):7566-7579.

[14] J. Zheng, W. Su, M. Fu. Dual-Stage Actuator Control Design Using a Doubly Coprime Factorization Approach. Mechatronics IEEE/ASME Transactions on, 2010, 15(3):339 - 348.

[15] Q. Xu, Design and Development of a Compact Flexure-Based Precision Positioning System With Centimeter Range. Industrial Electronics, IEEE Transactions on, 2014, 61(2): 893-903.

[16] A. Midha, T.W. Norton, L. L. Howell, On the nomenclature, classification, and abstractions of compliant mechanisms. Journal of Mechanical Design, 1994, 116(1): 270-279.

[17] F. Wang, X. Zhao, D. Zhang, Y. Wu, B. Shirinzadeh, Y. Tian. Design and control of a high-acceleration precision positioning system using a novel flexible decoupling mechanism. Proceedings of the Institution of Mechanical Engineers Part C Journal of Mechanical Engineering Science, 2010, 224(2):431-442.

[18] F. Wang, Z. Ma, W. Gao, X. Zhao, Y. Tian, D. Zhang, and C. Liang. Dynamic modeling and control of a novel XY positioning stage for semiconductor packaging", Transactions of the Institute of Measurement and Control, 2015, 37(2): 177-189.

[19] F. Wang, X. Zhao, D. Zhang, Z. Ma, X. Jing. Robust and precision control for a directly-driven XY table. Proceedings of the Institution of Mechanical Engineers Part C Journal of Mechanical Engineering Science, 2011, 225(5):1107-1120.

[20] Y. Tian, B. Shirinzadeh, D. Zhang, A flexure-based five-bar mechanism for micro/nano manipulation. Sensors and Actuators A: Physical, 2009, 153(1): 96-104.

[21] Y. K. Yong, T.-F. Lu, Kinetostatic modeling of 3-RRR compliant micro-motion stages with flexure hinges. Mechanism and Machine Theory, 2009, 44(6): 1156-1175.

[22] H. C. Liaw, B. Shirinzadeh, J. Smith, Robust motion tracking control of piezo-driven flexure-based four-bar mechanism for micro/nano manipulation. Mechatronics, 2008, 18(2): 111-120.

[23] M. N. M. Zubir, B. Shirinzadeh, Y. Tian, Development of a novel flexure-based microgripper for high precision micro-object manipulation. Sensors and Actuators A: Physical, 2009, 150(2): 257-266.

[24] Y.K. Yong, T.Y. Lu, The effect of the accuracies of flexure hinge equations on the output compliances of planar micro-motion stages. Mechanism and Machine Theory, 2008, 43(3): 347-363.

[25] Y. Tian, B. shirinzadeh, D. Zhang, Closed-form compliance equations of filleted V-shaped flexure hinges for compliant mechanism design. Precision Engineering, 2010, 34(3): 408-418.

[26] Y. Wu, Z. Zhou, Design calculations for flexure hinges. Review of Scientific Instruments, 2002, 73(8): 3101-3106.

[27] B. Trease, Y. Moon, S. Kota, Design of large-displacement compliant joints. Journal of mechanical design, 2005, 127(4): 788-798.

[28] H. Wang, X. Zhang, Input coupling analysis and optimal design of a 3-DOF compliant micro-positioning stage. Mechanism and Machine Theory, 2008, 43(4): 400-410.

[29] S. Polit, J. Dong, Development of a high-bandwidth XY nanopositioning stage for high-rate micro-/nanomanufacturing. Mechatronics, IEEE/ASME Transactions on, 2011, 16(4): 724-733.

[30] Y. Li and Q. Xu, Design and robust repetitive control of a new parallel-kinematic XY piezostage for micro/nanomanipulation. Mechatronics, IEEE/ASME Transactions on, 2012, 17(6): 1120-1132.

[31] S. Dejima, W. Gao, K.Katakura, S. Kiyono, Y. Tomita, Dynamic modeling, controller design and experimental validation of a planar motion stage for precision positioning. Precision Engineering, 2005, 29(3): 263-271.

[32]G. Hao, X. Kong, A novel large-range XY compliant parallel manipulator with enhanced out-of-plane stiffness. Journal of Mechanical Design, 2012, 134(6): 061009.

[33]Y. Koseki, T. Tanikaw, N. Koyachi, N. Arai and T. Arai, Kinematic analysis of a translational 3-dof micro-parallel mechanism using the matrix method. Advanced Robotics,2002, 16(3):251-264.

[34]S. Awtar, Synthesis and analysis of parallel kinematic XY flexure mechanisms. PhD Thesis, Massachusetts Institute of Technology, 2003.